Soil Dynamics and Earthquake Engineering 151 (2021) 106955

Contents lists available at ScienceDirect

Soil Dynamics and Earthquake Engineering

journal homepage: www.elsevier.com/locate/soildyn

Performance-based probabilistic assessment of liquefaction-induced building settlements

Chenying Liu [a], Jorge Macedo [a,*], Gabriel Candia [b]

[a] Georgia Institute of Technology, United States
[b] Universidad del Desarrollo, Chile, and National Research Center for Integrated Natural Disaster Management ANID/FONDAP/15110017, Santiago, Chile

ARTICLE INFO

Keywords:
Liquefaction-induced settlements
Performance-based design
Settlement hazard curves
Probabilistic seismic hazard assessment

ABSTRACT

The current state of practice in the estimation of liquefaction-induced building settlements (LIBS) relies on pseudoprobabilistic approaches in which the estimation of ground motion intensity measures (IMs) is separated from the estimation of LIBS. In contrast, in a performance-based probabilistic approach, the estimation of the IM hazard is coupled with the estimation of the LIBS hazard. Thus, engineers can obtain LIBS estimates that are directly related to a selected design hazard level (or return period), which is more consistent with performance-based design.

In this study, we present new developments for the performance-based probabilistic evaluation of LIBS, including 1) the performance-based assessment of LIBS considering the hazard from a single IM in the context of scalar probabilistic seismic hazard assessment (PSHA), 2) the performance-based assessment of LIBS considering the hazard from multiple IMs in the context of vector PSHA, 3) deaggregation of earthquake scenarios from LIBS hazard curves, 4) estimation of LIBS hazard curves in areas where earthquakes from multiple tectonic settings can occur (e.g., shallow crustal, subduction), and 5) treatment of uncertainties (i.e., aleatory and epistemic). The developments are implemented in a computational platform named "LIBS", which is fully coupled with PSHA assessments and facilitates the straightforward performance-based estimation of LIBS in engineering practice. Finally, we perform comparisons of performance-based and pseudoprobabilistic-based estimates of LIBS and share insights from the comparisons.

1. Introduction

Liquefaction-induced ground failure contributes significantly to earthquake damage. Ground that was solid before ground shaking can transform temporarily into a fully softened state with little strength and stiffness. In particular, liquefaction can induce damage in shallow founded buildings by producing significant building settlement and damage in previously stable buildings, which can tilt, deform, and collapse. Fig. 1 shows some examples of damage caused by liquefaction-induced building settlements (LIBS) in urban centers after recent earthquakes. LIBS has historically caused substantial damage in cities, notably San Francisco in 1906, Niigata in 1964, Adapazarı in 1999, Christchurch in 2010–2011, Urayasu in 2011, and Palu in 2018. For example, the 2010–2011 Canterbury, New Zealand earthquakes caused minor, moderate, or severe liquefaction damage depending on the particular event within the sequence. The earthquake sequence damaged more than 20,000 residential homes with huge economic impacts for New Zealand (Henderson, [1]). The 2011 Tohoku earthquake caused similar levels of liquefaction-induced damage to buildings, with about 27,000 houses damaged (Yasuda et al. [2]).

Macedo et al. [3] discuss the different frameworks for estimating engineering demand parameters (EDPs) when analytical models are available to evaluate an EDP of interest. These frameworks are categorized as deterministic, pseudoprobabilistic, and performance-based probabilistic. In a deterministic approach, an earthquake design scenario (i.e., a combination of earthquake magnitude - M_w and distance -R_{rup}) is first identified, often using the deaggregation results from a probabilistic seismic hazard assessment (PSHA). The identified M_w and R_{rup} are used as inputs into a ground motion model (GMM) to evaluate the ground motion intensity measure (IM) of interest. The estimated IM, along with soil and building properties, are used as inputs into a building settlement model to estimate LIBS. Often the uncertainty in the estimated LIBS is introduced through the standard deviation of the analytical LIBS model. In a pseudoprobabilistic framework, which currently

* Corresponding author.
E-mail address: jorge.macedo@ce.gatech.edu (J. Macedo).

https://doi.org/10.1016/j.soildyn.2021.106955
Received 8 February 2021; Received in revised form 29 July 2021; Accepted 26 August 2021

dominates in engineering practice, the IM of interest is estimated from a PSHA study that considers all the potential earthquake scenarios (not only one or few as in the deterministic framework). The PSHA study provides the annual rate of exceedance for different IM thresholds, also known as the IM hazard curve, which is used to select the IM of interest given a hazard design level. Once the IM is selected, the next steps are similar to those described before for the deterministic framework. In a performance-based probabilistic framework, a convolution between the entire IM hazard curve obtained from a PSHA study and a LIBS analytical model is performed. Hence, the uncertainties in the ground motion and properties of a geotechnical system can be considered. This is in contrast with the pseudoprobabilistic framework, where only one IM level is selected. One of the results of a performance-based assessment is a LIBS hazard curve, which provides the annual rate of exceedance for different LIBS thresholds. Thus, engineers can directly estimate the LIBS associated with a selected design hazard level (or return period), which is more consistent with performance-based engineering concepts as the design hazard is associated with the EDP of interest and not the IM. Performance-based methods do not assume a consistency between selected IM and EDP hazard design levels, which is implicit in pseudoprobabilistic frameworks. Instead, the entire IM hazard is used to estimate the EDP hazard. Macedo et al. [3] and Rathje and Saygili [4] provide additional discussions on the issues of the consistency assumption in pseudoprobabilistic assessments.

Despite the advantages of performance-based approaches, the current state of practice for the estimation of LIBS relies on deterministic or pseudoprobabilistic approaches. In general, this is also the case for other geotechnical earthquake engineering problems, where performance-based approaches are not commonly used in engineering practice because their implementation is often considered cumbersome. In addition, as discussed later, in the case of LIBS, only a few robust analytical models (i.e., formulated using a large number of realistic ground motions, building properties, and validated with cases histories) have been recently proposed, which justifies their use in pseudoprobabilistic approaches as a first step. However, a transition to performance-based approaches is also desirable.

In this study, we present new developments for the performance-based probabilistic assessment of liquefaction-induced building settlements, including 1) performance-based assessment of LIBS hazard curves for models that consider a single IM in the context of scalar PSHA, 2) performance-based assessments of LIBS for models that consider multiple IMs using vector PSHA, 3) deaggregation of earthquake scenarios directly from LIBS hazard curves, 4) integration of the ground motion hazard from different tectonic settings (i.e., shallow crustal and subduction) in the performance-based assessment of LIBS, 5) integration of aleatory variability and epistemic uncertainty through a logic tree approach.

We have implemented the new developments on a computational platform that facilitates the straightforward performance-based evaluation of LIBS in engineering practice. We are not aware of previous studies that have performed implementations that can directly accommodate earthquake scenarios and seismic sources like those found in engineering projects in the estimation of LIBS. Finally, we compare performance-based and pseudoprobabilistic approaches to estimate LIBS and share the insights from these comparisons, which we expect to be useful for engineering practice.

2. Previous studies on liquefaction-induced building settlements

Liquefaction of the soils supporting buildings with shallow foundations has caused severe damage to buildings during major earthquakes. The initial research efforts to understand the mechanisms associated with liquefaction-induced damage used shaking tables and centrifuge tests, considering saturated clean sand (loose to medium dense) deposits that supported rigid shallow foundations (e.g., Dashti [5], Liu and Dobry [6], Yoshimi and Tokimatsu [7]). These studies allowed researchers to broadly categorize the mechanisms associated with LIBS as shearing-induced, volumetric-induced, or ejecta-induced (e.g. Refs. [8, 9], and [10]). The different mechanisms associated with LIBS are schematically presented in Fig. 2.

Other researchers have also used advanced constitutive models in nonlinear dynamic soil-structure-interaction (SSI) effective stress analyses to understand liquefaction-induced building damage mechanisms better. These analyses have been generally used as benchmarks for the performance of buildings over liquefiable soils observed in centrifuge tests and well-documented case histories. (e.g., Luque and Bray [11],

Fig. 1. Examples of liquefaction-induced building settlement damage after recent earthquakes in (a) and (b) New Zealand, (c) Turkey, and (d) Chile. Adapted from Zupan [50], Bray et al. [41], Sancio [51], and Bertalot et al. [52].

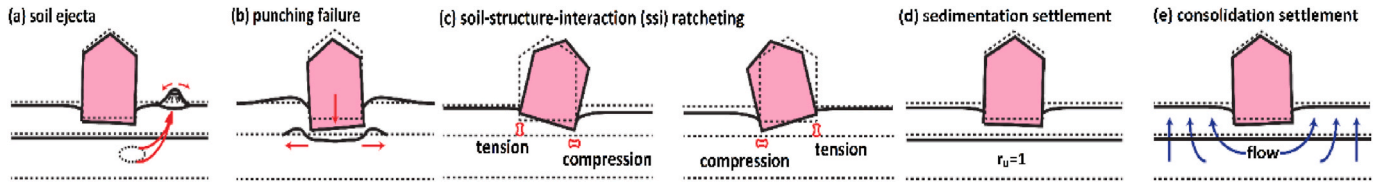

Fig. 2. Mechanisms associated with LIBS: settlements due to ground loss associated with (a) soil ejecta; shear-induced settlement from (b) loss of bearing capacity (e.g., punching failure), or (c) soil-structure-interaction (SSI) ratcheting; and volumetric-induced settlement from (d) sedimentation, or (e) post-liquefaction and reconsolidation (Bray et al. [10]).

Karimi and Dashti [12], Dashti and Bray [13], Karamitros et al. [14], Popescu et al. [15], Travasarou et al. [16], Elgamal et al. [17], Shakir and Pak [18]).

These additional research efforts have shown that nonlinear dynamic SSI effective stress analyses can capture many of the key aspects of the soil-structure interaction of buildings over liquefiable soils. Hence, nonlinear dynamic SSI effective stress analyses have also been used to formulate few analytical models to estimate LIBS (e.g., Karamitros et al. [14], Bray and Macedo [19], and Bullock et al. [20]). In this study, we use the Bray and Macedo [19] and Bullock et al. [20] models, henceforth referred to as BM2017 and B2018, respectively.

The BM2017 and B2018 models are robust analytical LIBS models. They have been developed considering a large number of realistic ground motions, several soil profiles and building configurations, soil-structure interaction with flexible buildings, and quantification of the uncertainty in the LIBS estimate, and validation against case histories.

The BM2017 model is based on a large set of numerical analyses by Macedo and Bray [21] using the PM4Sand constitutive model (Boulanger and Ziotopoulou [22]), and the B2018 model is based on a large set of numerical analyses by Karimi et al. [23] using the PDMY02 model (Elgamal et al. [24], Yang et al. [25]). Both the BM2017 and B2018 models are used as inputs for the performance-based developments performed in this study.

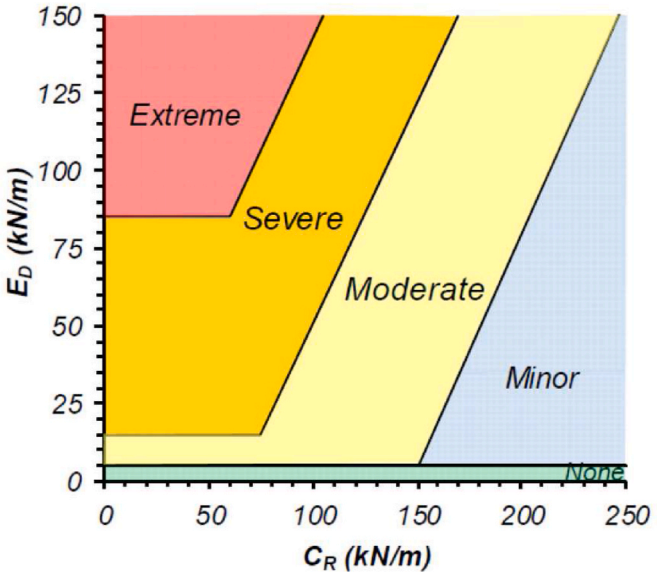

Fig. 3. Estimation of liquefaction-induced ejecta severity from C_R and E_D.

3. New developments for the performance-based assessment of liquefaction-induced building damage

This section presents the new developments and implementations for the performance-based assessment of LIBS.

3.1. Analytical LIBS models considered in this study

Predictive models for LIBS are generally formulated as a function of building parameters (**β**), soil properties (**θ**), and the ground motion IM. As previously mentioned, in this study, we use the BM2017 and B2018 models to estimate LIBS.

The BM2017 model estimates LIBS using Equation (1).

$$LIBS = D_s + D_v + D_e \tag{1}$$

where D_s, D_v, and D_e are the settlements associated with shearing, volumetric, and ejecta mechanisms in units of mm, respectively. The settlements associated with shearing mechanisms can be calculated using the model provided by Bray and Macedo [19] in Equation (2).

$$\ln D_s = c1 + 4.59 \ln Q - 0.42(\ln Q)^2 + c2 \cdot LBS + 0.58 \ln\left(\tanh\frac{HL}{6}\right) - 0.02B + 0.84 \ln CAV_{dp} + 0.41 \ln Sa_1 + \varepsilon \tag{2a}$$

$$LBS = \int_{D_f}^{z_{max}} \frac{\varepsilon_{shear}}{z} dz \tag{2b}$$

where ε_{shear} represents the shear strain in a soil layer, and it is calculated from Cone Penetration Test (CPTu) information (see Bray and Macedo [19]), z is the depth (m) from the surface to a soil layer (m), D_f is the depth (m) from the surface to the bottom of the foundation, z_{max} is the maximum depth (m) of a soil profile that can be important for liquefaction assessment, and *LBS* is an index that represents the potential of a soil profile to produce shear-induced deformations. The constants in Equation (2a) are $c1 = -7.48$ and $c2 = 0.014$ for $LBS > 16$ and $c1 = -8.35$ and $c2 = 0.072$ for $LBS \leq 16$. The term *HL* is the cumulative thickness (m) of layers with $FS_L \leq 1.0$, where FS_L is the safety factor for liquefaction triggering. Q is the foundation contact pressure in the units of kPa, and B is the foundation width (m). CAV_{dp} (m/s) is a modified version of the cumulative absolute velocity (*CAV*) defined by Campbell and Bozorgnia [26], $Sa1$ (g) is the spectral acceleration (*Sa*) at 1 s, and ε is a random variable with zero mean and standard deviation $\sigma_{lnDs} = 0.5$

(in natural logarithm units).

The settlement induced by volumetric mechanisms, D_v, is estimated using the procedure proposed by Juang et al. [27]. This procedure provides a mean estimate and standard deviation (σ_{lnDv}) for D_v using standard CPTu information (i.e., tip resistance, friction sleeve, and pore pressure readings). Equations for estimating D_v and σ_{lnDv}, provided by Juang et al. [27] are included in the electronic Appendix A.

The estimation of D_e is challenging due to the complex mechanisms associated with ejecta and the uncertainty of quantifying it. In this study, we adopt the procedure proposed by Hutabarat [28], where the likelihood of ejecta and its induced settlements are estimated from the CPTu-based parameters E_D (liquefaction ejecta demand index) and C_R (crust resistance index), which are used in the ejecta severity chart shown in Fig. 3. In this chart, the regions ' None', 'Minor', 'Moderate', 'Severe', and 'Extreme' refer to ejecta-induced settlements of 0 mm, 0 to 50 mm, 50 to 100 mm, 100 to 300 mm, and larger than 300 mm, respectively. A summary of the equations used to evaluate E_D and C_R is included in the electronic Appendix B.

The B2018 model estimates LIBS using a soil layering and soil properties inferred from standard penetration test (SPT) or CPTu data, building parameters, and *CAV* as the ground motion IM. The formulation of this procedure is presented in Equation (3).

$$\ln LIBS = f_{so} + f_{fnd} + f_{st} + s_0 \ln CAV + k_0 + k_1 \min\left(H_{S,1}, 12\right)^2 + k_2 \min(Q,\ Q_c) + k_3 \max(Q - Q_c, 0) \tag{3a}$$

$$f_{so} = \sum_i H\left(H_{S,i} - 1 + \varepsilon\right) f_{S,i} f_{H,i} + (c_0 + c_1 \ln CAV) F_{LPC} \tag{3b}$$

$$f_{S,i} = \begin{cases} a_0, & q_{c1N,i} < 112.4 \\ a_0 + a_1\left(q_{c1N,i} - 112.4\right), & 112.4 \le q_{c1N,i} < 140.2 \\ a_0 + 27.8a_1, & 140.2 \le q_{c1N,i} \end{cases} \tag{3c}$$

$$f_{H,i} = b_0 H_{S,i} \exp\left(b_1 \left(max\left(D_{S,i}, 2\right)^2 - 4\right)\right) \tag{3d}$$

$$f_{fnd} = f_Q + f_{B,L} \tag{3e}$$

$$f_Q = \{d_0 + d_1 \ln[\min(CAV, 1000)]\} \ln Q \exp\left(d_2 \min\left(0, B - \max\left(D_{S,1}, 2\right)\right)\right) \tag{3f}$$

$$f_{B,L} = (e_0 + e_1 \ln(\max(CAV, 1500))) \cdot (\ln B)^2 + e_2(L/B) + e_3 D_f \tag{3g}$$

$$f_{st} = (f_0 + f_1 \ln(\min(CAV, 1000)))h_{eff}^2 + f_2 \min\left(\left(M_{st} / 10^6\right), 1\right) \tag{3h}$$

In these equations, $H(\cdot)$ is the Heaviside step function, $q_{c1N,\,i}$ is the normalized CPTu tip resistance for layer i as defined by Robertson and Wride [29], ε is a very small positive number, F_{LPC} is a flag that is equal to 1 if a low-permeability layer is present above the uppermost susceptible layer, $H_{S,i}$ is the thickness (m) of the i-th susceptible layer, $D_{S,i}$ is the depth (m) from the bottom of the foundation to the center of the i-th susceptible layer, Q, D_f, and B are already defined; L/B is the length-to-width ratio of the foundation; $D_{S,1}$ is the depth (m) to the center of the uppermost susceptible layer, h_{eff} is the effective height (m) of the structure, and M_{st} is the inertial mass of the structure (kg). The remaining terms k_0, k_1, k_2, k_3, Q_c, a_0, a_1, b_0, b_1, c_0, c_1, d_0, d_1, d_2, e_0, e_1, e_2, e_3, f_0, f_1, f_2, s_0 are constants defined in Bullock et al. [20]. In this model, the standard deviation for LIBS is 0.67.

3.2. Performance-based assessment of LIBS

The computation of settlement hazard is obtained by adding the probability of exceeding a given settlement threshold level s weighted by the rate of occurrence of IM, which implies a convolution of the seismic hazard and a LIBS model. For instance, consider a tectonic setting with *Ns* seismic sources and a LIBS model formulated in terms of a single IM and no explicit magnitude (M_w) dependence. The settlement hazard curve is obtained by adding the contribution of each seismic source as shown in Equation (4), where the superscript k denotes the k-th realization of epistemic uncertainty in the form of alternative: (i) seismic hazard curves, (ii) building parameters, and (iii) soil properties.

$$\lambda_{EDP}^k(s) = -\sum_{i=1}^{Ns} \int_{IM} P\left(EDP > s \middle| im, \boldsymbol{\beta}^k, \boldsymbol{\theta}^k\right) \Delta\lambda_{IM}^{i,k}\, d(im) \tag{4}$$

In Equation (4), $\lambda_{EDP}^k(s)$ is the annual rate of exceedance of EDP at threshold s for the k-th realization of epistemic uncertainty, im is a realization of IM, $\Delta\lambda_{IM}^{i,k} = \frac{d\lambda_{IM}^{i,k}}{d(im)}$ is the derivative of the IM hazard curve in the i-th source, $\boldsymbol{\beta}^k$ is the k-th realization of building parameters, and $\boldsymbol{\theta}^k$ is the k-th realization of soil properties based on different CPTu interpretation methods. The term $P\left(EDP > s \middle| im, \boldsymbol{\beta}^k, \boldsymbol{\theta}^k\right)$ is the probability that the engineering demand parameter EDP exceeds a threshold level s, conditioned on $\boldsymbol{\beta}^k, \boldsymbol{\theta}^k$ and the ground motion level im. If the predictive model for settlement has an explicit dependence on M_w (e.g., as in the volumetric strain deformation model by Juang et al. [27]), the settlement hazard curve can be evaluated using Equation (5).

$$\lambda_{EDP}^k(s) = -\sum_{i=1}^{N_s} \sum_{j=1}^{N_m} \int_{IM} P\left(EDP > s \middle| im, m_j, \boldsymbol{\beta}^k, \boldsymbol{\theta}^k\right) P_M\left(m_j \middle| im\right) \Delta\lambda_{IM}^{i,k} d(im) \# \tag{5}$$

where m_j is M_w value representing the j-th magnitude bin, and the conditional probability $P_M(m_j|im)$ can be estimated from the IM hazard deaggregation. The deaggregation is conducted over N_m magnitude values sampled between a minimum and maximum M_w, which are specific to each seismic source. Similarly, the settlement hazard for models defined in terms of two or more intensity measures, say IM_1, IM_2, …IM_n, can be computed from the n-dimensional integral in Equation (6); in this case, $\mathbf{IM} = [IM_1\ IM_2 \ldots IM_n]^T$, $\mathbf{im} = [im_1\ im_2 \ldots im_n]^T$ represents a realization of **IM,** and $\Delta\lambda_{\mathbf{IM}}^{i,k} = \partial\lambda_{\mathbf{IM}}^{i,k}/\partial(\mathbf{im})$ is the joint rate of occurrence for **IM** obtained from a vector PSHA.

$$\lambda_{EDP}^k(s) = -\sum_{i=1}^{N_s} \sum_{j=1}^{N_m} \int_{\mathbf{IM}} P\left(EDP > s \middle| \mathbf{im}, m_j, \boldsymbol{\beta}^k, \boldsymbol{\theta}^k\right) P_M\left(m_j \middle| \mathbf{im}\right) \Delta\lambda_{\mathbf{IM}}^{i,k} d^n\mathbf{im} \tag{6}$$

Equations (4)–(6) provide the settlement hazard for a single realization of the epistemic uncertainty. Thus, in a logic tree with N_k realizations to account for epistemic uncertainties (i.e., N_k branches and weighting factors w_k), the mean hazard is computed directly as the weighted sum of hazard curves λ_{EDP}^k, as shown in Equation (7).

$$\lambda_{EDP}(s) = \sum_{k=1}^{N_k} \lambda_{EDP}^k(s) w_k \tag{7}$$

In terms of the developments performed as part of this study, the estimation of the LIBS hazard when the B2018 model is used considers Equation (6), where IM = *CAV*, $\boldsymbol{\beta}_k = [B, L, D_f, Q, M_{st}]$ are the building properties, and $\boldsymbol{\theta}_k = [q_{c1Nj},\ H_{sj}, D_{sj}]$ are layer dependent properties derived from the CPTu log for the j-th layer; more details on our proposed approach to evaluate $\boldsymbol{\theta}_k$ when the B2018 model is used are described in the next section. The BM2017 model requires the estimation of the volumetric (D_v), shearing (D_s), and ejecta (D_e) components of settlement. Equation (7) implemented in the Juang et al. [27] procedure is used to estimate the settlement hazard associated with D_v, where IM = *PGA* (peak ground acceleration), and $\boldsymbol{\theta}_k = [\varepsilon_{vol\,j},\ PL_j]$, which are layer-dependent properties derived from the CPTu log for the j-th layer representing the volumetric strain and the liquefaction probability for the j-th layer. These parameters are estimated according to the procedures in Juang et al. [27]. Equation (8) implemented in the Bray and Macedo [19] analytical model is used to estimate settlement hazard curves associated with D_s, where IM = $[CAV_{dp}, PGA, Sa1]$ and $\boldsymbol{\beta}_k$ =

$[B, D_f, Q]$ are the building properties, and $\boldsymbol{\theta}_k = [LBS,\ HL]$ represent the soil properties and are derived from CPTu information. In terms of the vector hazard assessment involved in Equation (6), when the BM2017 model is used, this study uses the coefficients of correlation between *PGA* and *Sa*1 based on Baker and Jayaram [30] for shallow crustal settings and Macedo and Liu [31] for subduction settings. The coefficients of correlation between CAV_{dp} and *PGA/Sa*1 are estimated as part of this study using the procedure in Macedo et al. [32]. Appendix E presents the details of the estimated correlation coefficients. Elaborating more on CAV_{dp}, there are three filters, associated to CAV_{std} , *Sa*, and *PSV* (pseudo-spectral velocity) that define CAV_{dp} zero values (Campbell and Bozorgnia, [26]); but some researchers relax the *PSV* filter (e.g., Bray and Macedo, [19]; Campbell and Bozorgnia, [26]). In this study, we follow the suggestions in Campbell and Bozorgnia [26]- see section 6.2 - of ignoring the *Sa* and *PSV* checks; in addition, we ignore the CAV_{std} check (i.e., instances where CAV_{dp} is zero).

These considerations are expected to provide a conservative estimate of the CAV_{dp} hazard at low CAV_{dp} values, which would translate into conservative estimates of the LIBS hazard for low LIBS values (associated with low CAV_{dp} values), which we consider acceptable from a practical perspective as the performance for low CAV_{dp} values is expected to be acceptable. The assumption of not considering CAV_{dp} zero values is further explored in Appendix D using Monte Carlo simulations.

LBS_k and HL_k realizations are estimated using the Boulanger and Idriss [33] and the Robertson and Wride [29] liquefaction triggering procedures with equal weights of 0.5 to account for epistemic uncertainties.

Finally, given the complexities and uncertainties associated with ejecta-based mechanisms, we estimate D_e as follows. For a given performance objective defined in terms of a return period T_r, we estimate the mean *PGA* and its deaggregated M_w, which are used to estimate r_u (excess pore pressure ratio) and FS_L, which then serve as inputs to estimate D_e using the Hutabarat [28] procedure, through the calculation of E_D and C_R.

In the context of the BM2017 procedure, we also estimate hazard curves that combine the volumetric and shearing mechanisms. Recall that the shear and volumetric components (i.e., D_s and D_v) that go into the Bray and Macedo [19] procedure correspond to two lognormal random variables developed independently. Their sum is also a random variable with mean D (Equation (8a)) and standard deviation σ_D (Equation (8b)).

$$D = \exp\left(\ln D_s + 0.5\sigma^2_{\ln Ds}\right) + \exp\left(\ln D_v + 0.5\sigma^2_{\ln Dv}\right) \tag{8a}$$

$$\boldsymbol{\sigma_D} = \sqrt{\left(\exp(\boldsymbol{\sigma^2_{\ln Ds}}) - 1\right)\exp(2\ln \boldsymbol{D_s} + \boldsymbol{\sigma^2_{\ln Ds}}) + \left(\exp\left(\boldsymbol{\sigma^2_{\ln Dv}}\right) - 1\right)\exp\left(\ln \boldsymbol{D_v} + \boldsymbol{\sigma^2_{\ln Dv}}\right)} \tag{8b}$$

For convenience, we treat the distribution of the added shear and volumetric components as an equivalent lognormal distribution, which has also been a consideration suggested by other researchers (e.g., Bullock et al., [34]). In this procedure, the mean ($\mu_{\ln LIBS}$) and standard deviation ($\sigma_{\ln\ LIBS}$) of the equivalent distribution are obtained by solving the following system of equations.

$$\begin{aligned} \exp\left(\ln LIBS + 0.5\sigma^2_{\ln LIBS}\right) &= D \\ \left(\exp\left(\sigma^2_{\ln LIBS}\right) - 1\right)\exp\left(2\ln LIBS + \sigma^2_{\ln LIBS}\right) &= \sigma^2_D \end{aligned} \tag{9}$$

Once $\mu_{\ln LIBS}$ and $\sigma_{\ln\ LIBS}$ are estimated, Equation (6) is used to evaluate settlement hazard curves that consider the combined effect of volumetric and shearing mechanisms. The corresponding IMs, $\boldsymbol{\beta}_k$, and $\boldsymbol{\theta}_k$ inputs used in all the procedures just described are summarized in Table 1. In Appendix D, we assess the Wilkinson's approach [35] as an alternative to approximate the lognormal distribution, and we also evaluate the lognormality assumption by performing Monte Carlo simulations. The results suggest that the lognormal approximation is reasonable and practical.

Table 1
Summary of the settlement formulations used in the current study.

Settlement Component	Integrate with Equation	**IM**	$\boldsymbol{\beta}_k$	$\boldsymbol{\theta}_k$
LIBS (Bullock et al. [20])	(3)	*CAV*	B, L, D_f, Q, M_{st}	$q_{c1N,i}$, $H_{s,i}$, $D_{s,i}$
Volumetric (Juang et al. [27])	(5)	*PGA*	–	$\varepsilon_{vol,i}$, PL_i
Shear (Bray & Macedo [19])	(6)	CAV_{dp},*PGA*, *Sa*1	B, D_f, Q	*LBS*, *HL*
LIBS (Bray & Macedo [19])	(6–9)	CAV_{dp},*PGA*, *Sa*1	B, D_f, Q	$\varepsilon_{vol,i}$, PL_i, *LBS*, *HL*

3.3. Treatment of soil properties using CPTu information

The B2018 method requires a layering of the soil profile. In this study, we implement a procedure that combines a Markov Random Field (MRF) and a Gaussian mixture model for an automated layering of the soil profile using CPTu information. The details of the algorithm employed in this study are presented in Wang et al. [36]. The discrete CPTu measurements are grouped into different clusters (layers) according to their similarity in spatial and statistical patterns in the implemented procedure. Specifically, the spatial patterns refer to the distribution of soil types across the depth of a CPTu sounding, in which it is assumed that closely located measurements are more likely to belong to the same soil type than those far away from each other. The statistical patterns describe the distribution of CPTu measurements in a CPTu soil type chart (e.g., Robertson and Cabal [37]). Accordingly, the spatial patterns and statistical patterns of CPTu measurements are modeled as a Markov Random Field (MRF) and a Gaussian mixture model. Jointly, both patterns are integrated into a Gaussian hidden MRF, as shown in Fig. 4.

In Fig. 4, the CPTu measurements are plotted in a CPTu soil type chart; a Gaussian mixture model is used to fit the CPTu measurements to form a multi-modal distribution with K clusters (e.g., K = 2 in the schematic example of Fig. 4). Then, for the *i*-th measurement there is a corresponding latent random variable x_i, representing the potential cluster the *i*-th measurement belongs to, which takes value from 1 to K. y_i is a two-dimensional random vector, which consists of ($q_{c1N,i}$, $F_{r,i}$) for the *i*-th CPTu measurement, where $q_{c1N,i}$, and $F_{r,i}$ are the normalized tip resistance, and normalized friction resistance, respectively. Using x_i, y_i, and the spatial and statistical patterns embedded in the Gaussian hidden MRF, an automatic layering of the CPTu profile can be performed. Additional mathematical details of this procedure are included in Appendix C. The procedure just described has been implemented in the computational platform developed as part of this study. This procedure is used in the illustrative examples presented later.

3.4. Deaggregation of earthquake scenarios from LIBS hazard curves

Let's consider that the contributions from earthquake scenarios and ground motion scenarios to an IM hazard level in Equation (4) are binned in *nM* values of M_w, *nR* values of R_{rup}, and *nε* values of epsilon (ε), where ε is the number of standard deviations above the median IM in the generation of IM realizations in Equation (4). This results in a total $nScen = nM \cdot nR \cdot n\varepsilon$ ground motion scenarios. Let's also consider *nIM* threshold levels for IM, and *nlibs* threshold levels for LIBS in Equation (4). Under these considerations, the contributions to the IM hazard can be stored in a matrix $[\lambda_{IM}]$ with *nScen* rows and *nIM* columns, and the annual rate of occurrence $\Delta\lambda_{IM}$ in Equation (4) can be approximated as:

$$\Delta\lambda_{IM} = -\frac{d\lambda_{IM}}{d(IM)} \approx -\frac{\lambda_{IM_j} - \lambda_{IM_{j+1}}}{IM_j - IM_{j+1}} = -\frac{RO_{IM}}{IM_j - IM_{j+1}} \tag{10}$$

where $RO_{IM} = \lambda_{IM_j} - \lambda_{IM_{j+1}}$, is the rate of occurrence of the ground motion

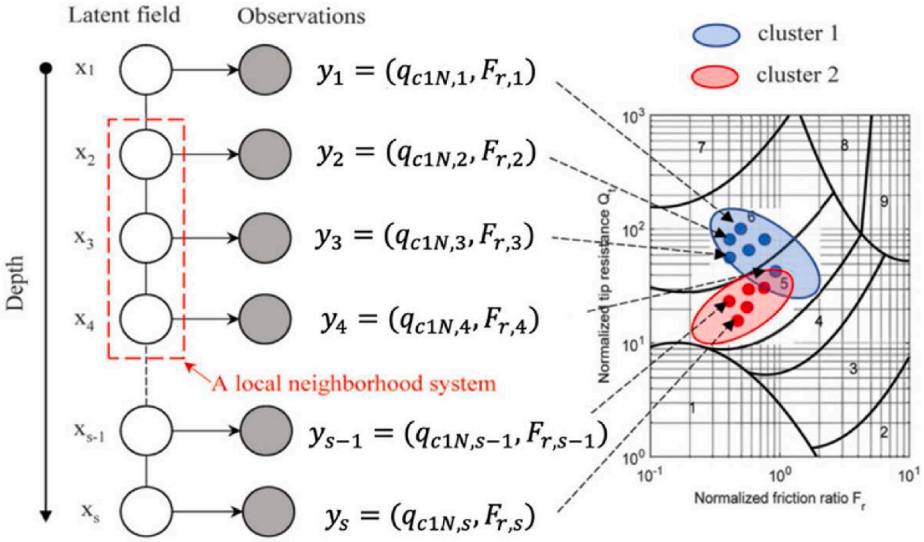

Fig. 4. Illustration of the Gaussian hidden MRF model for soil layering using CPTu information. Adapted from Wang et al. [36].

intensity IM_j, and the operations are performed with components of the matrix $[\lambda_{IM}]$. Hence, another matrix $[\Delta\lambda_{IM}]$ containing the rates of occurrence for different scenarios can also be defined. To ensure that $[\Delta\lambda_{IM}]$ and $[\lambda_{IM}]$ have the same dimensions, the *nIM*-th column of $[\Delta\lambda_{IM}]$ is made a duplicate of its $(nIM-1)$-th column. Now, considering a fixed LIBS level, and fixed $\boldsymbol{\beta}^k$, $\boldsymbol{\theta}^k$ parameters, we can evaluate Equation (4) for each ground motion scenario and at each IM level. This will result in a matrix $[\lambda_{LIBS_p}]$ with *nScen* rows and *nIM* columns that contain partial contributions to the LIBS rates of occurrences sorted by ground motion scenarios and IM values. Finally, the contribution to the LIBS hazard from all IM levels is estimated by summing up the columns of $[\lambda_{LIBS_p}]$, which will result in a vector of length *nScen* denoted as $[\lambda_{LIBS}]$ that can be used as a proxy to perform the deaggregation of the LIBS hazard curve as follows:

$$[\lambda_{LIBS}] = [\lambda_{LIBS1}, \lambda_{LIBS2}, \ldots, \lambda_{LIBSnScen}]^T,\ Deagg_{LIBS_i} = \lambda_{LIBS_i} \Big/ \sum_{p=1}^{nScen} \lambda_{LIBS_p} \tag{11}$$

In Equation (11), $Deagg_{LIBS_i}$ represents the LIBS hazard deaggregation for the *i*-th earthquake scenario. This information can be used to evaluate the scenarios that dominate LIBS from a LIBS hazard curve. Because the earthquake scenarios are evaluated from the LIBS hazard and not the IM hazard, this procedure is more consistent with performance-based engineering.

3.5. Estimation of LIBS hazard curves considering multiple tectonic settings

In some cases, a building could be affected by earthquakes from different tectonic settings; for example, a building on the South American coast or in the Pacific Northwest is expected to be affected by shallow crustal and subduction type (i.e., interface, intraslab) earthquakes. Let's consider that a particular area is potentially affected by earthquakes from N_s^{SC}, N_s^{SI}, N_s^{SS} shallow crustal, subduction interface, and subduction intraslab seismic sources. Through a PSHA study, the contributions from different tectonic settings to the total IM hazard can be evaluated. According to Equation (4), the contributions to the total IM hazard are denoted as λ_{IM}^{SC} from shallow crustal settings, λ_{IM}^{SI} from subduction interface settings, and λ_{IM}^{SS} from subduction intraslab settings. The annual rate of occurrences $\Delta\lambda_{IM}^{SC}$, $\Delta\lambda_{IM}^{SI}$, and $\Delta\lambda_{IM}^{SS}$ for each tectonic setting can also be estimated from Equation (10). The total LIBS hazard curve can now be evaluated according to:

$$\lambda_{EDP}^{total} = \lambda_{EDP}^{SC} + \lambda_{EDP}^{SI} + \lambda_{EDP}^{SS} \tag{12}$$

where λ_{EDP}^{SC}, λ_{EDP}^{SI}, and λ_{EDP}^{SS} correspond to the deaggregated LIBS hazard curves by tectonic mechanisms and can be estimated from Equations (4)–(6), depending on the selected LIBS model's formulation for each tectonic setting. Equation (12) has been implemented in the computational platform developed as part of this study, which is discussed in the "implementations" section.

In terms of the models used in this study, the BM2017 model has been formulated using ground motions from shallow crustal tectonic settings, and the B2018 used ground motions from shallow crustal and subduction tectonic settings but with a predominance of ground motions from shallow crustal earthquakes. In evaluating the trends of the B2018 model for different tectonic settings, the authors notice that they did not observe major differences. Importantly, both the BM2017 and the B2018 models have been formulated as conditional models, i.e., the estimation of settlements is conditioned on IMs. Thus, until new settlement models that are specific for subduction settings are formulated, we suggest incorporating the effect of different tectonic settings into the settlement estimate through the use of adequate GMMs to estimate the IMs for the tectonic setting of interest. This means that λ_{IM}^{SC}, λ_{IM}^{SI}, and λ_{IM}^{SS} should be estimated using GMMs formulated for shallow crustal, subduction interface, and subduction intraslab, respectively. This is the approach followed in the second illustrative example (see the illustrative examples section). The robustness of conditional models for different tectonic settings has also been observed in conditional GMMs formulated for secondary IMs (e.g., Macedo et al. [38]).

4. Implementations

We have implemented the procedures described in previous sections in a computational MATLAB-based graphical user interface platform denominated as "LIBS", which greatly simplifies the estimation of settlement hazard curves in engineering practice. The implemented hazard framework accounts for the variability and uncertainties on the ground motion intensities (aleatory and epistemic), building properties (if required), as well as treatment of soil profiles required for the estimation of LIBS.

The software LIBS has several distinctive capabilities, which allow the evaluation of LIBS hazard curves considering realistic seismic sources and multiple tectonic settings (i.e., shallow crustal and

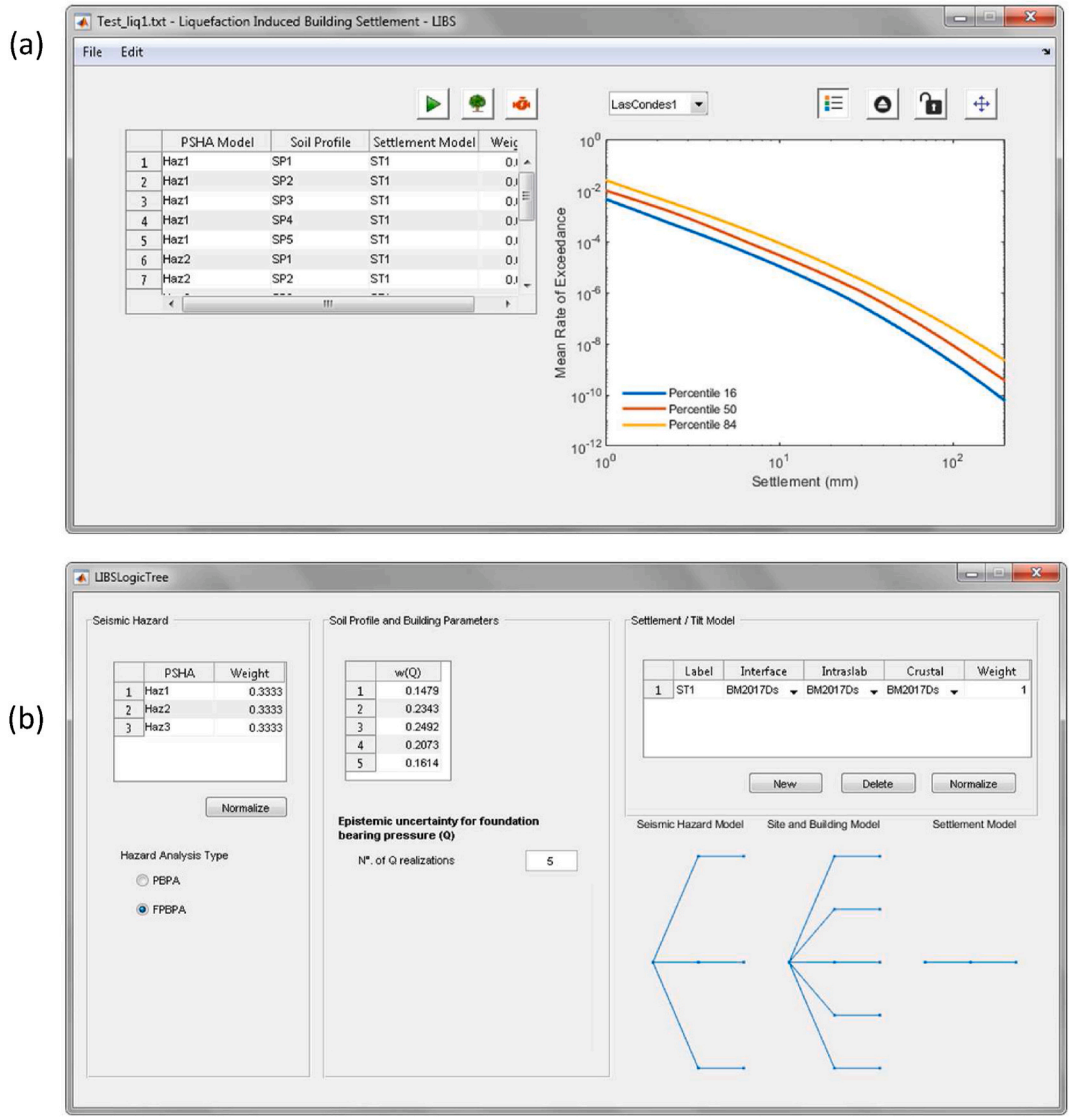

Fig. 5. Graphical user interface for the performance-based estimation of liquefaction-induced building settlements: (a) main panel for results visualization, and (b) logic tree explorer.

subduction settings).

The user interface has four main modules or panels; the opening module (Fig. 5a) shows a summary of the logic tree branches used to compute settlements and displays the resulting settlement hazard curves after the calculations are completed. The second module (Fig. 5b) allows inspecting and editing the logic tree structure, including the seismic hazard branches, building and soil profile properties, the epistemic uncertainty parameters used in the BM2017 and B2018 models, as well as the settlement formulation used in the different tectonic settings. The remaining modules (not shown here) allow visualizing the settlement models, the input CPTu data, and the automatic layering from the Gaussian hidden MRF model previously discussed. The platform can be accessed through GitHub at https://github.com/gacandia/LIBS.

The platform has an embedded state-of-the-art software for seismic hazard assessment, which provides a full coupling between the estimation of LIBS hazard curves and PSHA evaluations, which is desired in engineering practice. The embedded seismic hazard toolbox (see full documentation in Candia et al. [39,40] has a built-in library of over 60 GMMs for subduction and shallow crustal settings, including the latest GMMs for multiple IMs such as *PGA*, *PGV* (peak ground velocity), *Sa*, *CAV,* and *AI* (Arias Intensity). The software features built-in seismicity models for Chile, Perú, México, and Ecuador and allows to import user-defined models through text files.

5. Illustrative examples and comparisons between pseudoprobabilistic and performance-based approaches

In this section, we present two illustrative examples for the application of the performance-based procedures discussed in previous sections. We consider the subsurface soil information for the building FTG-7, which was affected by the 2011 Christchurch earthquake. We use the CPTu log referred to as CPT-Z1-B3 in Bray et al. [41], which provides information on the subsurface conditions at this site. The subsurface profile consists of 1–1.5 m thick fill at the ground surface, underlain by a shallow sandy silt/silty sand (SM/ML) layer with variable FC (fines content) and I_c (material index) generally between 2.2 and 2.4, which extends down to a depth of 7–8.5 m (Bray et al. [41], and Bray and Macedo, [42]). Below this layer, a medium dense sand (SP/SM, $I_c \approx 1.8$ and 2.1) is found, which extends down to a depth of around 14 - 16.5 m. The loose SM/ML layer below the groundwater table (located at 2 m depth) and soil units in the SP/SM layer are likely to liquefy under strong shaking. Below the medium dense sand, a very dense sand (SP) layer is encountered. The CPTu typically reaches refusal in this unit. Finally, there is a dense gravel at approximately 22 m depth, which is overlaid by

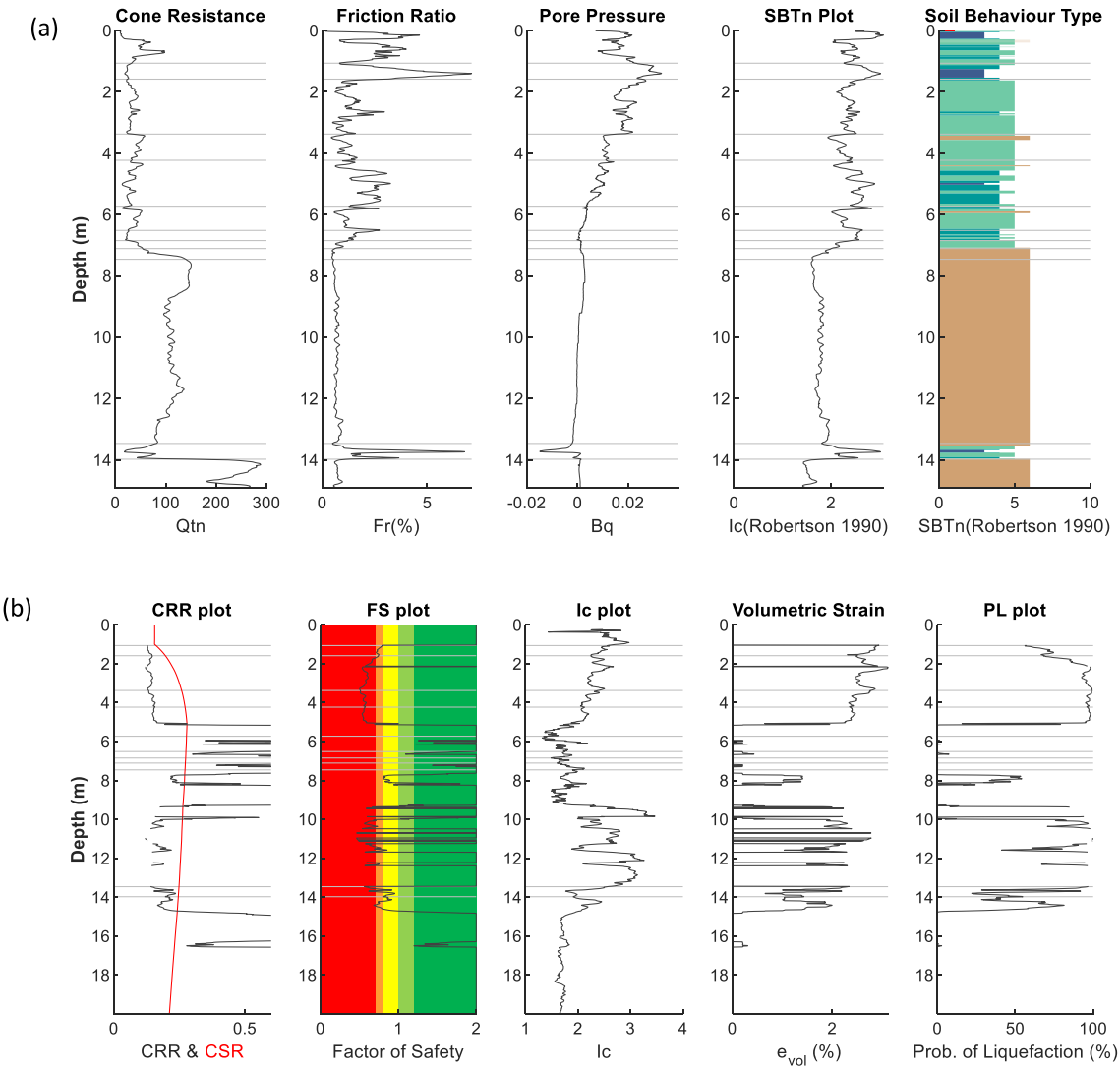

Fig. 6. (a) Normalized CPTu data for CPT-Z1-B3, and (b) liquefaction triggering results for a magnitude 7 earthquake and $PGA = 0.24$ g at site CPT-Z1-B3 obtained from the Boulanger and Idriss [33] procedure. Horizontal lines indicate the layering obtained using the Gaussian-MRF procedure discussed in the text. All plots are generated with the computational platform implemented in this study. I_c and SBT (Soil Behavior Type) are estimated according to Robertson [53]. (CRR and CSR are the cyclic resistance ratio and cyclic stress ratio. FS is the factor of safety for liquefaction triggering and PL is the probability of liquefaction.). Different colors in the soil behavior type plot in Fig. 6a indicate different SBTn values, and different colors in Fig. 6b and c indicate different safety factor ranges. (For interpretation of the references to color in this figure legend, the reader is referred to the Web version of this article.)

a 1 - 2 m thick clayey silt (ML/MH) layer with some organics. Fig. 6 shows salient features from the CPT-Z1-B3 CPTu and the layering (shown using horizontal lines) evaluated automatically using the Gaussian hidden MRF described before. These results are obtained from the platform implemented as part of this study.

In our analyses, we use the same hypothetical building considered by Bullock et al. [20], consisting of a six-story reinforced concrete building supported on a 10 m by 20 m mat foundation embedded 2 m below the ground surface. The building parameters required for the application of the BM2017 and B2018 procedures are: $Q = 91.3$ kPa, $B = 10$ m, $D_f = 2$ m, $L/B = 2$ m, and $M_{st} = 1.861 \times 10^6$ kg.

5.1. Example considering shallow crustal seismicity

We consider a single seismic source and two magnitude recurrence scenarios, referred to as MR1 and MR2, which differ in the source's activity rate and the slope of the magnitude recurrence relationship. The source is a rectangular strike-slip fault (strike = 0°, dip = 90°, width = 30 km, length = 105 km), with the south end located 20 km west of the

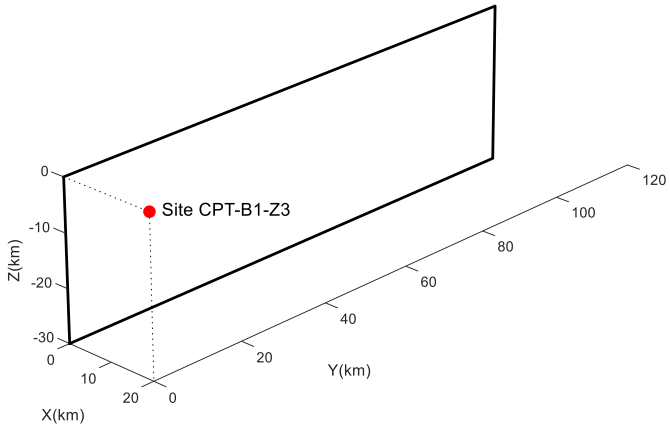

Fig. 7. Source geometry and site location, herein the Y-axis runs south-north.

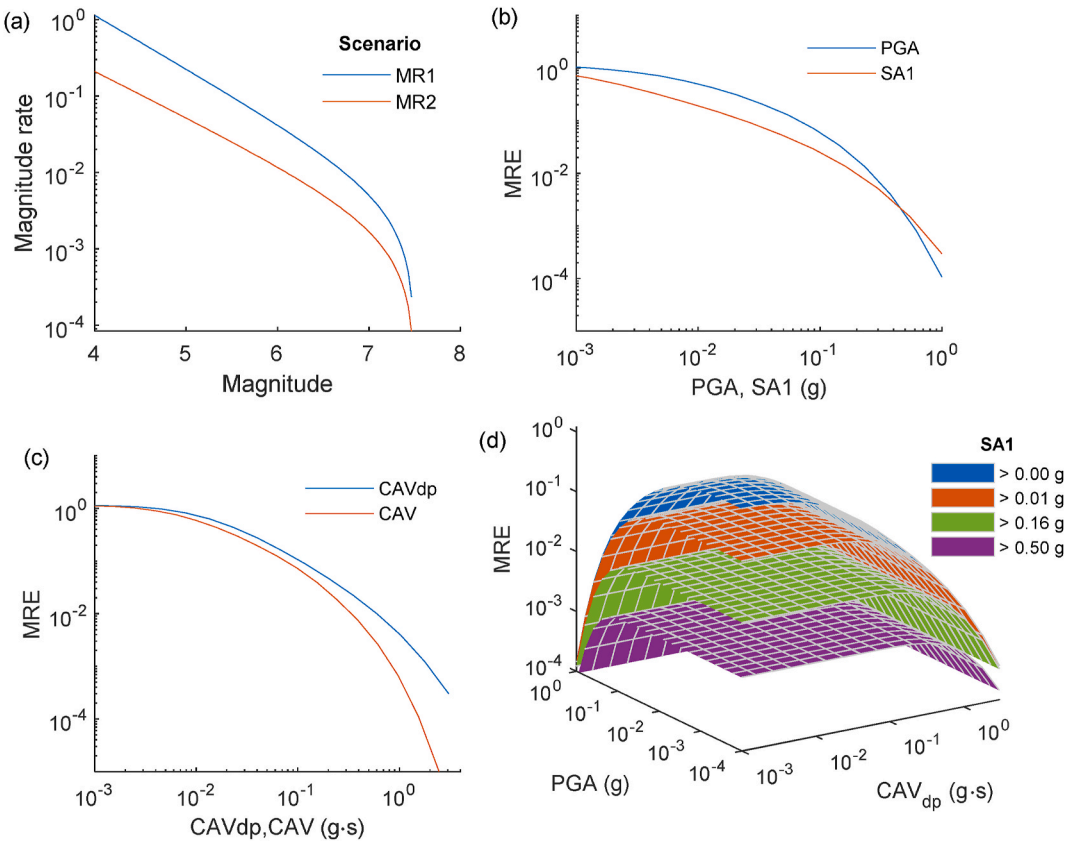

Fig. 8. (a) Guttenberg Richter relation for the two scenarios considered; hazard results for MR1: (b) *PGA* and *Sa*1 hazard curves; (c) CAV_{dp} and *CAV* hazard curves; (d) surfaces of the multivariate *PGA*, *Sa*1, and CAV_{dp} hazard.

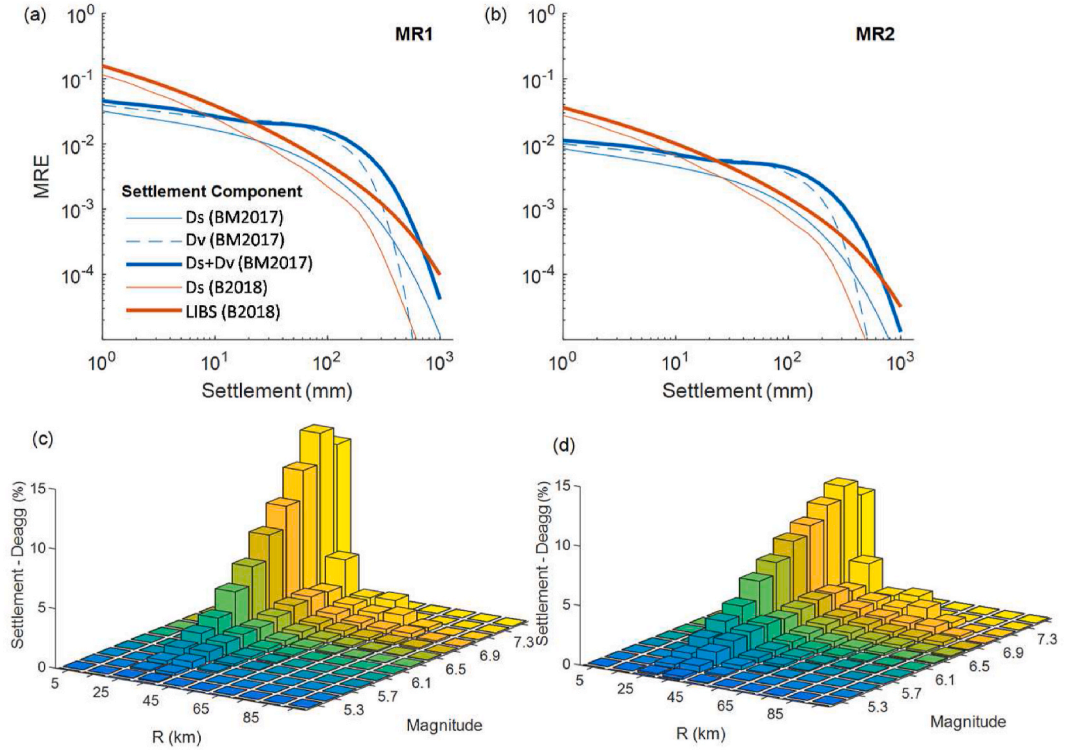

Fig. 9. Settlement hazard curves at site CPT-Z1-B3 for the two magnitude recurrence scenarios (a) MR1 and (b) MR2. M_w- R_{rup} hazard deaggregation of the 475 yr return period settlement for earthquake scenarios (c) MR1, ($LIBS_{475}$ = 205 mm, mean(M_w) = 6.9, and mean(R_{rup}) = 28.9 km), and (d) MR2 ($LIBS_{475}$ = 70 mm, mean (M_w) = 6.7, and mean(R_{rup}) = 32.5 km).

building, as illustrated in Fig. 7.

The magnitude recurrence law is represented by a truncated exponential distribution with moment magnitudes between 4.0 and 7.5, b-values of 0.7 and 0.6, and activity rates of 1.13 and 0.21 events per year for scenarios MR1 and MR2, respectively. On average, these sources generate a magnitude 7.0 earthquake every 200 years and 600 years, respectively. The magnitude recurrence relations are shown in Fig. 8a. In our implementation of the BM2017 model, the seismic hazard accounts for jointly occurring *PGA*, *Sa*1, and CAV_{dp}, then a vector-PSHA has been employed, which we have implemented according to Equation (6) in the LIBS platform. In the case of the B2018 model, only the *CAV* scalar hazard is required.

We use the V_{s30} = 270 m/s of the soil profile (V_{s30} is the time-averaged shear-wave velocity in the top 30 m, required in the GMMs) to estimate the seismic hazard, as required in the BM2017 procedure. In terms of GMMs, we use the Campbell and Bozorgnia [43] GMM for *PGA* and *Sa*1, the Campbell and Bozorgnia [26] GMM for CAV_{dp}. The *CAV* hazard required for the B2018 procedure is estimated using the Macedo et al. [32] GMM. Of note, the *CAV* hazard curve is estimated using a V_{s30} of 760 m/s as required by the B2018 model. All these GMMs can be accessed through the LIBS platform implemented in this study. Fig. 8b shows the individual mean *PGA* and *Sa*1 hazard curves, whereas Fig. 8c shows the individual mean *CAV* and CAV_{dp} hazard curves. An example of the vector hazard results in terms of the annual rate of exceedance surfaces is shown in Fig. 8d for the recurrence scenario MR1. Each surface in Fig. 8d represents the joint annual rate of exceedance of *PGA* and CAV_{dp} for *Sa*1 ranges. Fig. 9 shows the settlement hazard curves calculated for the two scenarios considered. In the case of the BM2017 model, we present settlement hazard curves that combine shearing and volumetric mechanisms as well as deaggregated hazard curves by settlement mechanism (i.e., shearing and volumetric). Of note, the ejecta-induced settlement is estimated using the Hurabarat [28] procedure considering the *PGA* values and deaggregated magnitudes for 475 and 2475 years of return periods evaluated from the hazard curves in Fig. 8b and added to the $D_s + D_v$ estimate for the hazard level being evaluated, as previously discussed (section: performance-based assessment of LIBS). In addition, in Appendix D, we examine the sensitivity of the $D_s + D_v$ hazard curves to the correlation between shearing and volumetric components, which can be incorporated by using the Wilkinson's approach ([35]). This is performed by varying the correlation coefficient from 0 to 1, with results presented in Appendix D. We find that the correlation coefficient affects the hazard curves at large settlement values, but not significantly (see Figure D.3). Fig. 9 also shows the hazard curves from the B2018 model, considering the total settlements and the contribution from shearing mechanisms.

It can be observed that the settlement hazard curves calculated using the BM2017 model have significant contributions from volumetric mechanisms for both the MR1 and MR2 scenarios. The contribution from ejecta is also significant (see Table 2), and it is influenced by the soil conditions considered for this example. Table 2 presents the contribution from different mechanisms considering the scenarios MR1 and MR2 and return periods of 475 and 2475 years. It is important to mention that the estimation of the contributions from volumetric and ejecta-induced settlements to the total settlement in the BM2017 procedure depends on the adopted models for these mechanisms. In this example, the contributions from these mechanisms have been evaluated using the Juang et al. [27] method for volumetric settlements (which is an update of the Zhang et al. [44] method) and the Hutabarat [28] method for ejecta-induced settlements. The contribution from ejecta is stable (59 mm) for the two scenarios (MR1 and MR2) and different return periods. This is because the Hutabarat [28] procedure includes a cap for r_u at $FS_l = 1.0$ (see the equations in Appendix B). Thus, if comparable portions of the soil profile have a $FS_l < 1.0$ for different scenarios/return periods, the ejecta estimate is not significantly affected.

Table 2
Example 1: LIBS estimates considering a performance-based approach and the BM2017, B2018 models.

Return Period (yr)	Scenario	Performance Based Settlement (mm)						
		BM2017				B2018		
		D_s	D_v	D_e	LIBS	D_s	$D_v + D_e$	LIBS
475	**MR1**	152	268	59	400	104	156	210
	MR2	48	160	59	220	37	43	70
2475	**MR1**	355	370	59	650	255	305	560
	MR2	203	294	59	450	155	138	292

In the B2018 model, the contribution of mechanisms other than shearing (e.g., volumetric, ejecta) to the total settlements is comparable to the contributions from shearing mechanisms for both 475 and 2475 years of return periods. Remember that the B2018 model lumps up the contribution from any mechanisms that are different from shearing through a correction based on case histories. Hence, we use their predictive equation before correction to estimate the contribution from shearing mechanisms. In addition, Bullock et al. [20] only provide models to estimate either the total settlement or the shear-induced settlement probabilistically (i.e., using the framework discussed in this study), but they do not provide a model with associated uncertainties for non-shearing mechanisms. Thus, the settlement hazard curves in Fig. 9 (and subsequent figures) only consider hazard curves for D_s and *LIBS*. The D_s estimates using the Bray and Macedo [19] procedure are approximately 1.35 times (on average) larger than the D_s estimates from the Bullock et al. [20] for both MR1 and MR2 scenarios, and this ratio is approximately stable for the two return periods of 475 and 2475 years being considered.

Table 2 also includes the results of LIBS estimates for 475 and 2475 years of return periods. The BM2017 procedure provides larger estimates compared to the B2018 model, but the estimates from these two procedures indicate a similar performance. For example, the estimates for the MR1 scenario vary from 210 to 400 for 475 years of return period and from 560 to 650 for 2475 years of return period. These estimates indicate that the building performance will likely be poor in the two cases. Thus, both the BM2017 and B2018 procedures are useful in estimating LIBS as a performance index. Finally, Fig. 9c and d show the deaggregation of earthquake scenarios obtained from B2018-based LIBS hazard curves for the MR1 and MR2 scenarios. For example, considering the MR1 scenario, the earthquakes that contribute more to the LIBS hazard are associated with M_w between 6.5 and 7.0 and R_{rup} between 25 and 40 km.

We also estimate settlements using a pseudoprobabilistic approach, where hazard-consistent IMs are obtained from PSHA and used directly as input into the settlement BM2017 and B2018 models. In the case of the BM2017 model, the *PGA,* and CAV_{dp} values are obtained directly from their hazard curves at the return period of interest. The *Sa*1 is conditioned on *PGA* using the conditional mean spectrum approach (Baker, [45]). In the case of the B2018 model, the *CAV* values are obtained directly from its hazard curve at the return period of interest. The *PGA*, CAV_{dp}, *Sa*1, and *CAV* values estimated in this manner are presented in Table 3, along with the results from the pseudoprobabilistic assessments. The difference between the performance-based and pseudoprobabilistic estimates is quantified using the parameter $\Delta = Ln(LIBS_{PB}) - Ln(LIBS_{PP})$, where $LIBS_{PB}$ and $LIBS_{PP}$ are the settlement estimates from performance-based and pseudoprobabilistic approaches, respectively. In terms of the results using the B2018 model, the LIBS estimates from the performance-based assessment are higher than those from the pseudoprobabilistic assessment; hence, Δ is positive. Furthermore, Δ is higher in the MR1 scenario compared to the MR2 scenario because of the higher seismic activity in the MR1 scenario, which derives in larger $\Delta\lambda_{IM}$ values in Equation (6), causing more contribution to the annual rate of exceedance for a given LIBS value. Thus, the LIBS estimates in a performance-based approach depend on the entire *CAV* hazard curve.

Table 3
Example 1: IM values used in the pseudoprobabilistic estimates of LIBS and LIBS estimations considering the BM2017 and B2018 models.

Return Period (yr)	Scenario	Intensity Measures						Pseudo-Prob. Settlement (mm)							δ	
								BM 2017				B2018			BM 2017	B2018
		Mw	R_{rup}	*CAV*	CAV_{dp}	*PGA*	*Sa*1	D_s	D_v	D_e	LIBS	D_s	$D_v + D_e$	LIBS		
475	**MR1**	6.45	23.3	0.67	1.40	0.46	0.26	173	233	59	481	87	56	142	−0.18	0.39
	MR2	6.25	23.3	0.40	0.73	0.29	0.18	63	144	59	273	32	21	53	−0.21	0.27
2475	**MR1**	6.65	28.1	1.12	2.76	0.73	0.45	402	242	59	727	211	135	346	−0.11	0.48
	MR2	6.45	23.3	0.80	1.73	0.52	0.28	217	239	59	533	125	80	205	−0.17	0.35

This cannot be incorporated in a pseudoprobabilistic approach that relies on only one *CAV* value. Importantly, the LIBS estimates from a pseudoprobabilistic approach are not directly related to a return period. For example, consider the MR1 scenario; the current state of practice would assume that selecting *CAV* for a return period of 475 years would lead to a LIBS estimate consistent with 475 years. However, the LIBS estimate from the pseudoprobabilistic approach (142 mm) is actually associated with a return period of approximately 300 years (obtained from the LIBS hazard curve). Finally, Δ tends to increase as the return period increases. This can be illustrated by taking the MR1 scenario and considering the annual activity rate of earthquakes at a magnitude 7.0 of 1/200. For a median ground motion (i.e., its probability of exceedance is 0.5) the annual rate of exceedance for the median ground motion will be about 1/400 per year (i.e., 0.5 times 1/200). Thus, as the annual rate of exceedance departs more from 1/400 (i.e., the return period gets larger than 400 years) Δ tends to increase as ground motions larger than the median (which occur less frequently) go more often into the LIBS hazard curve. In terms of the results using the BM2017 model, the LIBS estimates from performance-based assessments are comparable but lower than those from pseudoprobabilistic assessments. In this case, the performance-based assessments are influenced by the joint rate of occurrence of three intensity measures (*PGA*, *Sa*1, and CAV_{dp}), which makes it difficult to make more direct comparisons.

5.2. Example considering a subduction tectonic setting and a logic tree

In this example, two Chilean seismic sources (one for subduction interface and another for subduction intraslab) are used to illustrate the calculations of LIBS hazard curves with contributions from multiple tectonic settings, which is feasible through the embedded seismic hazard capabilities of the implementations developed in this study. Consider the building and site properties from the previous example, but in this case, located in Santiago, Chile (Lon: -70.683°; Lat: -33.5424°), which is

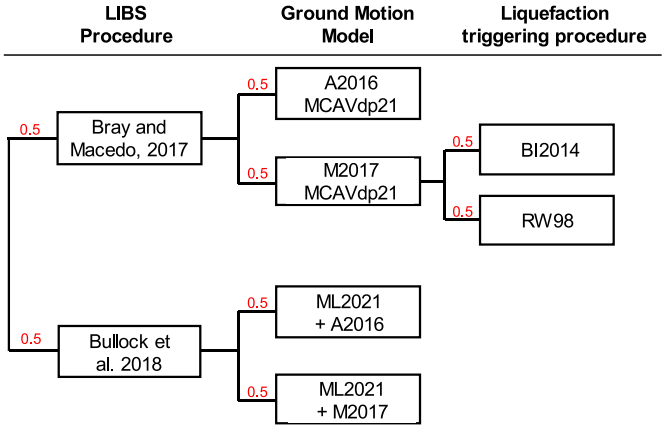

Fig. 11. Logic tree used to estimate LIBS hazard curves in the Chilean subduction setting. GMMs used are the Abrahamson et al. [47] (A2016), the Montalva et al. [48] (M2017), and the Macedo and Liu [49] (ML2021) models. Liquefaction triggering procedures includes the Boulanger and Idriss [33] (BI2015) and Robertson and Wride procedures [29] (RW98).

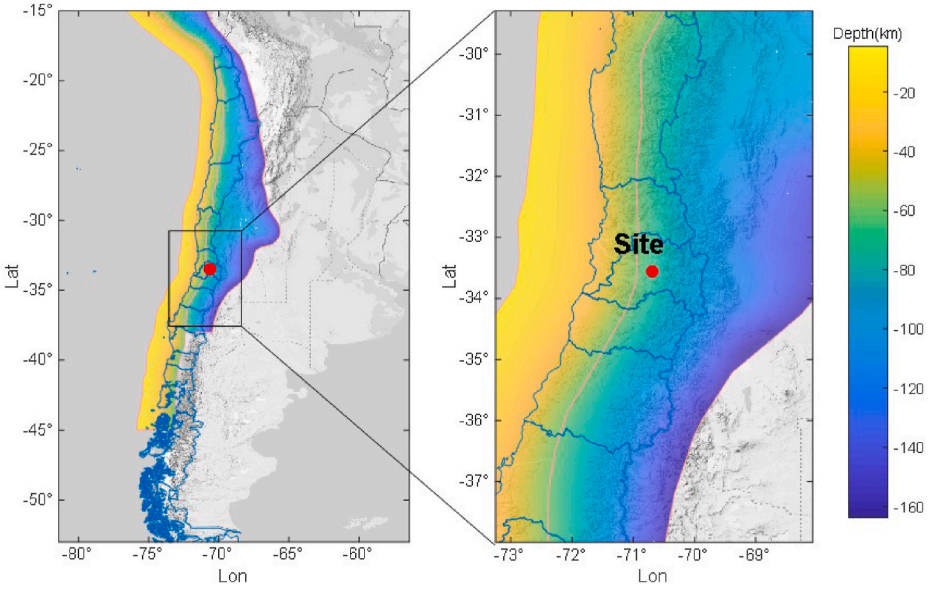

Fig. 10. Subduction interface and intraslab seismic sources for the Chilean seismic environment. Depths up to 50 km indicate an interface seismic source, and deeper depths are associated with the intraslab seismic source. Blue lines correspond to administrative boundaries. (For interpretation of the references to color in this figure legend, the reader is referred to the Web version of this article.)

affected by large megathrust earthquakes along the Peru-Chile trench and also by subduction intraslab earthquakes. We use the geometry and Guttenberg-Richter parameters defined by Poulos et al. [46] for the seismic sources, as illustrated in Fig. 10. Fig. 11 shows the logic tree employed in this example to illustrate the treatment of epistemic uncertainties. In terms of LIBS procedures, we consider the BM2017 and the B2018 procedures equally weighted. In the BM2017 procedures, we consider the Abrahamson et al. [47] and Montalva et al. [48] GMMs equally weighted for *PGA* and *Sa*1; CAV_{dp} considers two scenario-based implementations, equally weighted, of the conditional *CAV* model from Macedo and Liu [49] combined with the Abrahamson et al. [47], and Montalva et al. [48] GMMs. Finally, the triggering procedure to calculate LIBS considers the Boulanger and Idriss [33] and Robertson and Wride [29] methods equally weighted. The B2018 procedure considers scenario-based implementations of the *CAV* conditional model from Macedo and Liu [49], combined with the Abrahamson et al. [47] and Montalva et al. [48] GMMs.

The scalar hazard curves for these four intensity measures are shown in Fig. 12a and b. Similar to the previous example, the *PGA*, *Sa*1, and CAV_{dp} hazards are estimated for a V_{s30} value of 270 m/s, and the *CAV* hazard for a V_{s30} value of 760 m/s. Fig. 12c illustrates surfaces obtained through vector hazard analyses required for the BM2017 model; Fig. 12d presents comparisons between settlement hazard curves obtained with the BM2017 and B2018 models. Table 4 summarizes the results from performance-based assessments.

The LIBS estimates from the B2018 model are larger than the LIBS estimates from the BM2017 model. However, both procedures are useful in indicating a poor performance of the building for 475 years and 2475 years of return period. For instance, the LIBS estimates vary from 843 to 1357 mm for 475 years of return period and from 1373 to 2700 mm for 2475 years of return period. In terms of the BM2017 procedure, the contribution from volumetric and ejecta mechanisms to the total settlements, in this case, are comparable (but less important) compared to the contributions from shearing mechanisms for the two return periods

Table 4
Example 2: LIBS estimates considering a performance-based approach and the BM2017, B2018 models.

	Performance Based Settlement (mm)						
Return Period (yr)	BM2017				B2018		
	Ds	Dv	De	LIBS	Ds	Dv + De	LIBS
475	522	352	59	843	596	761	1357
2475	1052	448	59	1373	1073	1627	2700

of 475 and 2475 years considered. In terms of the B2018 model, the contributions of volumetric and ejecta mechanisms are larger than the contributions from shearing but still comparable. In addition, the D_s estimates from the BM2017 procedure are, in this case, slightly lower than the D_s estimates from the B2018 procedure (on average 95%), which is in contrast with the previous example where the BM2017 estimates were larger.

Fig. 13a presents deaggregation of LIBS hazard curves by tectonic mechanisms by using the B2018 model, and Fig. 13b shows the deaggregation of earthquake scenarios for a return period of 475 years. The deaggregation of hazard curves by tectonic mechanisms (Fig. 13a) shows that the intraslab mechanism is more important for low return periods (i.e., lower than 475 years), and the contributions from the two tectonic mechanisms are comparable for larger return periods. The deaggregation by earthquake scenarios shows major contributions from earthquakes with M between 7.0 and 9.0 and R_{rup} between 75 and 150 km. Table 5 shows the estimates from pseudoprobabilistic analyses along with *PGA, Sa*1*,* CAV_{dp}*,* and *CAV* estimates used in these analyses. In terms of the B2018 model, the performance-based LIBS estimates are larger than the pseudoprobabilistic estimates and $\delta = Ln(LIBS_{PB}) - Ln(LIBS_{PP})$ also increases with the return period as in the previous example for the reasons previously discussed. The performance-based LIBS estimates from the Bray and Macedo [19] procedure are more

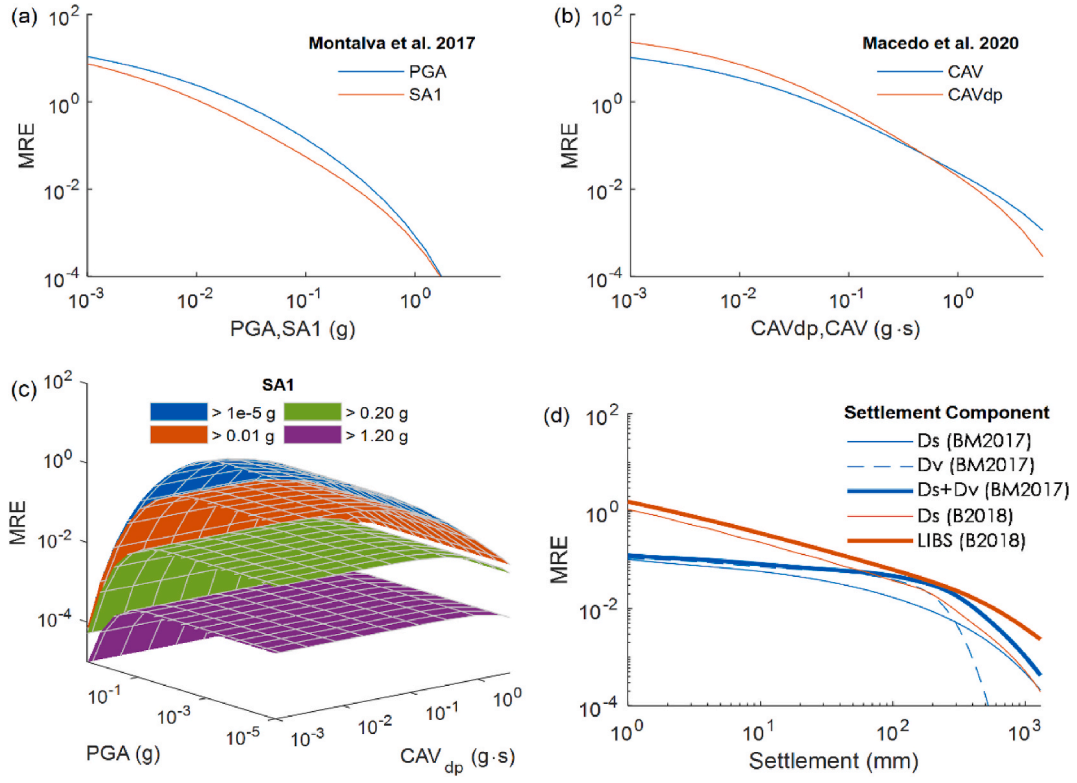

Fig. 12. Seismic hazard curves for (a) *PGA* and *Sa*1, (b) *CAV* and CAV_{dp}, (c) surfaces showing a jointly annual rate of exceedances for *PGA* and CAV_{dp} for given *Sa*1 ranges obtained through a vector hazard assessment, (d) settlement hazard curves obtained with the Bray and Macedo [19] and Bullock et al. [20] procedures.

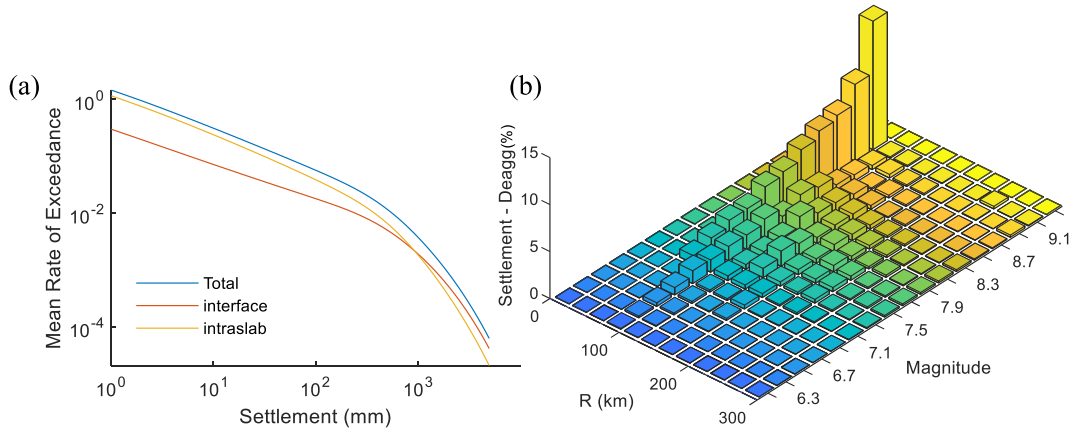

Fig. 13. (a) Settlement hazard curves deaggregated by mechanism, and (b) M_w-R_{rup} hazard deaggregation of the 475 yr return period settlement with $LIBS_{475}$ = 1357 mm, mean(M_w) = 8.1, and mean(R_{rup}) = 100 km.

Table 5
Example 2: IM values used in the pseudoprobabilistic estimates of LIBS and LIBS estimations considering the BM2017 and B2018 models.

							Pseudo-Prob. Settlement (mm)							Δ	
Return Period (yr)	Mw	R	CAV	CAVdp	PGA	SA1	BM2017				B2018			BM2017	B2018
	-	km	g•s	g•s	g	g	Ds	Dv	De	LIBS	Ds	Dv + De	LIBS		
475	8.1	65	2.7	3.0	0.5	0.2	508	242	59	834	530	341	870	0.01	0.44
2475	8.3	65	5.1	6.4	1.0	0.3	1029	242	59	1359	994	639	1633	0.01	0.50

comparable to those from pseudoprobabilistic assessments in this case. Finally, similarly to the previous example, the pseudoprobabilistic estimates from both the BM2017 and B2018 models cannot be directly related to a hazard design level or return period.

6. Conclusions

This study has presented new developments for the performance-based probabilistic assessment of liquefaction-induced building settlements (LIBS). All the developments have been implemented in a computational platform to facilitate their application in engineering practice. Performance-based approaches should be preferred in engineering practice because they better incorporate the uncertainties in the ground motion hazard, soil properties, and building properties. Furthermore, they can provide LIBS estimates directly related to a hazard design level (or return period). Hence, the assumption often considered in pseudoprobabilistic approaches, namely that the hazard level for an intensity measure (IM) is consistent with that of LIBS, is not anymore implied. The performance-based assessments discussed in this study enable a hazard-consistent estimate of LIBS, which is more rational as engineers should design for the expected LIBS given a hazard design level and not for the expected IM.

The performance-based implementations performed in this study consider the BM2017 and B2018 LIBS models. The BM2017 model is implemented in the context of a vector PSHA as it uses multiple IMs (PGA, $Sa1$, and CAV_{dp}). The soil properties are captured through the LBS index and the lumped thickness of liquefiable layers, for which epistemic uncertainties are considered by using two different liquefaction triggering procedures with equal weights in a logic tree approach. Alternative values for the building properties to represent their epistemic uncertainty could also be defined if required. The B2018 model is implemented using CAV hazard information in the context of scalar PSHA. Since the B2018 requires a layering of a soil profile as an input, a procedure based on a Gaussian hidden MRF process is used to generate automatic layering of soil profiles from a CPTu log. In the examples of this study, we use the median tip resistance from each layer, but other percentiles could also be used or even alternative weighted interpretations of the tip resistance in a logic tree scheme. Alternative building parameters could also be defined, if needed, as part of the epistemic uncertainty.

Considering the examples presented in this study, the performance-based estimates of D_s using the BM2017 and B2018 procedures are comparable (generally the D_s ratios from the two procedures are in the range of 0.9 to 1.4). However, there are differences in the final LIBS estimates, which depend on the tectonic settings and the return periods under consideration. Hence, the major differences between the BM2017 and B2018 procedures come from the differences in the contribution of non-shearing mechanisms (i.e., volumetric mechanisms and ejecta) to LIBS. These differences should be further explored in future studies, as more case histories that differentiate between different mechanisms become available. Even though there are differences between the BM2017 and B2018 procedures, they indicate consistent performance levels in the examples considered for this study (i.e., for high seismicity, both procedures provide large LIBS estimates that are indicative of poor building performance). Hence, we recommend using the two procedures equally weighted in engineering practice to account for the epistemic uncertainty in LIBS. In addition, we recommend using the B2018 method to deaggregate earthquake scenarios using the procedure proposed in this study. In the current state of practice, earthquake scenarios are deaggregated from IM hazard curves, but performing a deaggregation from LIBS hazard curves is more consistent with performance-based engineering concepts, which has also been highlighted in previous studies for slope systems (e.g., [54,55]).

In terms of comparisons between performance-based and pseudo-probabilistic procedures, the B2018 model provides larger LIBS estimates in the performance-based case, with the differences increasing as the return period increases and depending on the activity rate in the seismic sources being considered. Thus, the differences between

performance-based and pseudoprobabilistic procedures are expected to depend on the activity of seismic sources and the hazard design level (or return period) under consideration. In the case of the BM2017 procedure, the performance-based LIBS estimates are more comparable with the pseudoprobabilistic estimates in some scenarios. Because the BM2017 procedure uses multiple IMs performing direct comparisons between performance-based and pseudoprobabilistic approaches is complicated as the IMs are correlated and interact in the context of a vector PSHA.

Author Statement

Chenying Liu: Conceptualization, Software, Writing – original draft Jorge Macedo: Supervision, Conceptualization, Writing – original draft, Software. Gabriel Candia: Visualization, Software

Declaration of competing interest

The authors declare that they have no known competing financial interests or personal relationships that could have appeared to influence the work reported in this paper.

Acknowledments

The authors acknowledge the financial support from the Civil Engineering Department at Georgia Tech, through project number DE00000701, which made this study possible. Also, Dr. Candia has received financial support from Facultad de Ingeniería Civil at Universidad del Desarrollo, the National Research Center for Integrated Natural Disaster Management ANID/FONDAP/ 15110017, and FONDECYT Grant N°11180937 “Seismic Risk of Mined Tunnels”.

Appendix A. Supplementary data

Supplementary data to this article can be found online at https://doi.org/10.1016/j.soildyn.2021.106955.

References

[1] Henderson D. The performance of house foundations in the Canterbury earthquakes (Master’s thesis),” University of Canterbury. Civil and Natural Resources Engineering. http://ir.canterbury.ac.nz/handle/10092/8741; 2013.
[2] Yasuda S, Harada K, Ishikawa K, Kanemaru Y. Characteristics of liquefaction in Tokyo Bay area by the 2011 Great East Japan earthquake. Soils Found 2012;52(5):793–810.
[3] Macedo J, Bray J, Abrahamson N, Travasarou T. Performance-based probabilistic seismic slope displacement procedure. Earthq Spectra 2018;34(2):673–95.
[4] Rathje EM, Saygili G. Estimating fully probabilistic seismic sliding displacements of slopes from a pseudoprobabilistic approach. J Geotech Geoenviron Eng 2011;137(3):208–17.
[5] Dashti S. Toward developing an engineering procedure for evaluating building performance on softened ground. Berkeley: ” University of California; 2009.
[6] Liu L, Dobry R. Seismic response of shallow foundation on liquefiable sand. J Geotech Geoenviron Eng 1997;123(6):557–67.
[7] Yoshimi Y, Tokimatsu K. Settlement of buildings on saturated sand during earthquakes. Soils Found 1977;17(1):23–38.
[8] Bray JD, Dashti S. Liquefaction-induced building movements. Bull Earthq Eng 2014;12(3):1129–56.
[9] Dashti S, Bray JD, Pestana JM, Riemer M, Wilson D. Mechanisms of seismically induced settlement of buildings with shallow foundations on liquefiable soil. J Geotech Geoenviron Eng 2010;136(1):151–64.
[10] Bray J, Macedo J, Luque R. “Key trends in assessment of liquefaction-induced building settlement,” in *3rd international conference on performance-based design in earthquake geotechnical engineeing, Vancouver*. 2017.
[11] Luque R, Bray J. Dynamic analysis of a shallow-founded building in Christchurch during the Canterbury earthquake sequence. In: 6th international conference on earthquake geotechnical engineering; 2015.
[12] Karimi Z, Dashti S. Seismic performance of shallow founded structures on liquefiable ground: validation of numerical simulations using centrifuge experiments. J Geotech Geoenviron Eng 2016;142(6):04016011.
[13] Dashti S, Bray JD. Numerical simulation of building response on liquefiable sand. J Geotech Geoenviron Eng 2013;139(8):1234–49.
[14] Karamitros DK, Bouckovalas GD, Chaloulos YK. Seismic settlements of shallow foundations on liquefiable soil with a clay crust. Soil Dynam Earthq Eng 2013;46:64–76.
[15] Popescu R, Prevost JH, Deodatis G, Chakrabortty P. Dynamics of nonlinear porous media with applications to soil liquefaction. Soil Dynam Earthq Eng 2006;26(6–7):648–65.
[16] Travasarou T, Bray JD, Sancio RB. Soil-structure interaction analyses of building responses during the 1999 Kocaeli earthquake. In *100 th anniversary earthquake conference*. 2006.
[17] Elgamal A, Lu JaYZ. Liquefaction-induced settlement of shallow foundations and remediation: 3D numerical simulation. J Earthq Eng 2005;9(spec01):17–45.
[18] Shahir H, Pak A. Estimating liquefaction-induced settlement of shallow foundations by numerical approach. Comput Geotech 2010;37(3):267–79.
[19] Bray JD, Macedo J. 6th Ishihara lecture: Simplified procedure for estimating liquefaction-induced building settlement. Soil Dynam Earthq Eng 2017;102:215–31.
[20] Bullock Z, Karimi Z, Dashti S, Liel A, Porter K. Key parameters for predicting residual tilt of shallow-founded structures due to liquefaction. In: Geotechnical earthquake engineering and soil dynamics V: numerical modeling and soil structure interaction. VA: American Society of Civil Engineers Reston; 2018. p. 425–34.
[21] Macedo J, Bray J. Key trends in assessment of liquefaction-induced building settlements from numerical analyses. J Geotech Geoenviron Eng 2018;144(11).
[22] Boulanger R, Ziotopoulou K. PM4SAND (version 3): a sand plasticity model for earthquake engineering applications. Davis, Davis: ” Univ. of California; 2015.
[23] Karimi Z, Dashti S, Bullock Z, Porter K, Liel A. Key predictors of structure settlement on liquefiable ground: a numerical parametric study. Soil Dynam Earthq Eng 2017;113:286–308.
[24] Elgamal A, Yang Z, Parra E. Computational modeling of cyclic mobility and postliquefaction site response. Soil Dynam Earthq Eng 2002;22(4):259–71.
[25] Yang Z, Elgamal A, Parra E. Computational model for cyclic mobility and associated shear deformation. J Geotech Geoenviron Eng 2003;129(12):1119–27.
[26] Campbell K, Bozorgnia Y. Predictive equations for the horizontal component of standardized cumulative absolute velocity as adapted for use in the shutdown of U. S. nuclear power plants. Nucl Eng Des 2011;241(7):2558–69.
[27] Juang C, Ching J, Wang L, Khoshnevisan S, Ku C-S. Simplified procedure for estimation of liquefaction-induced settlement and site-specific probabilistic settlement exceedance curve using cone penetration test (CPT). Can Geotech J 2013;50(10).
[28] Hutabarat D. Effective stress analysis of liquefaction sites and evaluation of sediment ejecta potential. ” University of California of Berkeley; 2020.
[29] Robertson P, Wride C. Evaluating cyclic liquefaction potential using the cone penetration test. Can Geotech J 1998;35(3).
[30] Baker JW, Jayaram N. Correlation of spectral acceleration values from NGA ground motion models. Earthq Spectra 2008;24(1):299–317.
[31] Macedo J, Liu C. Ground-Motion Intensity Measure Correlations on Interface and Intraslab Subduction Zone Earthquakes Using the NGA-Sub Database. Bull Seismol Soc Am 2021;111(3):1529–41.
[32] Macedo J, Abrahamson N, Liu C. New Scenario-based cumulative absolute velocity models for shallow crustal tectonic settings. Bull Seismol Soc Am 2020;111(1):157–72.
[33] Boulanger R, Idriss I. CPT-based liquefaction triggering procedure. Journal of Geotechnical and Geoenvironmental Engineering; ASCE 2015;142(2).
[34] Bullock Z, Porter K, Liel AB, Dashti S. “ A framework for the evaluation of liquefaction consequences for shallow-founded structures,” in *13th international Conference on Applications of Statistics and Probability in civil engineering (ICASP13)*. Seoul: South Kore; 2019.
[35] Abu-Dayya A, Beaulieu N. Outage probabilities in the presence of correlated lognormal interferers. IEEE Trans Veh Technol 1994;43(1):164–73.
[36] Wang X, Wang H, Liang R, Liu Y. A semi-supervised clustering-based approach for stratification identification using borehole and cone penetration test data. Eng Geol 2019;248:102–16.
[37] Robertson P, Cabal K. Estimating soil unit weight from CPT. In: 2nd international symposium on Cone penetration testing, huntington beach, CA; 2010.
[38] Macedo J, Abrahamson N, Bray J. Arias intensity conditional scaling ground-motion models for subduction zones. Bull Seismol Soc Am 2019;109(4):1343–57.
[39] Candia G, Macedo J, Magna-Verdugo C. An integrated platform for seismic hazard assessment in subduction zones,” in *11th National conference on earthquake engineering*. Los Angeles: California; 2018.
[40] Candia G, Macedo J, Jaimes M, Magna-Verdugo C. A new state of the art platform for probabilistic and deterministic seismic hazard assessment. Seismol Res Lett 2019;90(6):2262–75.
[41] Bray J, Cubrinovski M, Zupan J, Taylor M. Liquefaction effects on buildings in the central business district of Christchurch. Earthq Spectra 2014;30(1):85–109.
[42] Bray J, Macedo J. Simplified Evaluation of Liquefaction-Induced Building Settlements. In: Geotechnical earthquake engineering and soil dynamics V. GEESD V) conference; 2018.
[43] Campbell K, Bozorgnia Y. NGA-West2 ground motion model for the average horizontal components of PGA; PGV; and 5% damped linear acceleration response spectra. Earthq Spectra 2014;30(3):1087–115.
[44] Zhang G, Robertson P, Brachman R. Estimating liquefaction-induced ground settlements from CPT for level ground. Can Geotech J 2002;39:1168–80.
[45] Baker J. Conditional Mean Spectrum: Tool for ground motion selection. J Struct Eng 2011;137(3):322–31.
[46] Poulos A, Monsalve M, Zamora N, de la Llera J. An updated recurrence model for Chilean subduction seismicity and statistical validation of its oisson nature an

updated recurrence model for Chilean subduction seismicity and statistical validation of its poisson nature. Bull Seismol Soc Am 2019;109(1):66–74.
[47] Abrahamson C, Shi M, Yang B. Ground-motion prediction equations for Arias intensity consistent with the NGA-West2 ground-motion models. " *PEER*; 2016. 2016/05 Report.
[48] Montalva G, Bastias N, Rodriguez-Marek A. "Ground-motion prediction equation for the Chilean subduction zone. Bull Seismol Soc Am 2017;107(2):901–11.
[49] Liu C, Macedo J. New conditional, scenario-based, non-conditional cumulative absolute velocity models for subduction tectonic settings. Earthquake Spectra; 2021. In press.
[50] Zupan JD. Seismic performance of buildings subjected to soil liquefaction. Berkeley: " University of California; 2014.
[51] Sancio RB. Ground failure and building performance in Adapazari, Turkey. Berkeley: " University of California; 2003.
[52] Bertalot D, Brennan A, Villalobos F. Influence of bearing pressure on liquefaction-induced settlement of shallow foundations. Geotechnique 2013;63(5):391–9.
[53] Robertson P. "CPT-based SBT classification system—an update. Can Geotech J 2016;53(12):1910–27.
[54] Macedo J, Candia G, Lacour M, Liu C. New developments for the performance-based assessment of seismically-induced slope displacements. Eng Geol 2020;277. https://doi.org/10.1016/j.enggeo.2020.105786.
[55] Macedo J, Candia G. Performance-based assessment of the seismic pseudo-static coefficient used in slope stability analysis. Soil Dynam Earthq Eng 2020;133. https://doi.org/10.1016/j.soildyn.2020.106109.